# Numerical simulation of different-scale fracture effects on saturation distributions in waterflooding via the finite volume method

Chao Tang [a, *], Wen Zhou [a], Zhimin Du [b], Zhangxin Chen [c], Jiabao Wei [d]

[a] State Key Laboratory of Oil and Gas Reservoir Geology and Exploitation, Chengdu University of Technology, Chengdu, Sichuan, 610059, China
[b] Department of Petroleum and Natural Gas Engineering, Southwest Petroleum University, Chengdu, Sichuan, 610500, China
[c] Department of Chemical and Petroleum Engineering, University of Calgary, Calgary, AB, T2N 1N4, Canada
[d] Sinopec Shengli Oilfield Company, Dongying, Shandong, 257000, China

## ARTICLE INFO

## ABSTRACT

Capturing the heterogeneity and multiple scales in fractured media is important for understanding the underlying mechanisms controlling the flow behavior, as both natural and hydraulic fractures can dominate the flow patterns in media of this type. Fracture characteristics, such as heterogeneity, multiple scales, and extreme size-to-aperture ratios, challenge standard macroscale mathematical and numerical modeling methods of the flow based on the concept of volume averaging. This paper presents a finite volume method approach for solving a two-phase flow model of discrete fractures that accounts for the heterogeneity and multiscale fracture distribution in fractured reservoirs. Fracture model combinations, obtained by restricting different models to different parts of a domain or by using models with explicit representations of fractures as a basis for upscaled continuum models, are also presented. Furthermore, the model error correction method due to fracture dimensionality reduction and an inappropriate up-wind scheme is also analyzed.

Crown Copyright © 2021 Published by Elsevier Ltd. All rights reserved.

## 1. Introduction

Natural fractures are very common geological structures, and they are widely distributed in all kinds of strata. Almost all reservoirs are affected by natural fractures to some extent [1]. Furthermore, the stimulation of hydraulic fracturing creates many hydraulic fractures. Both natural and hydraulic fractures have an important effect on the percolation performances of oil and gas reservoirs. Thus, since the 1960s, the description and modeling of fracture networks have been a popular topic of research, and a large number of scholars have devoted many efforts to these concepts. A more detailed discussion of some of the aspects of fracture modeling can be found in previously published books [2–5] and review articles [6–8]. However, because of the difficulty and complexity of the flow mechanisms, some problems still have not been effectively solved [8].

Matrix media generate fractures under the action of a mechanical load and environmental factors (e.g., leaching and dissolution). Once fractures are generated, expanded, and connected, they become channels for mass and energy exchange between the media and their surroundings, which has a significant influence on the permeability of the media. Thus, the purpose of the numerical simulation of fractured reservoirs is to clarify the distribution of fracture networks and then study the flow dynamics in these reservoirs.

In previous studies, different conceptual models suitable for fractured reservoirs have been proposed based on representations of fractured porous media, which mainly included implicit and explicit representation models. The simplest implicit representation of fractures is named the Single Continuum Model, which represents fractures by adapting the permeability (equivalent permeability) of a single porous medium. Mozolevski et al. [9] proposed a method for calculating the equivalent permeability of fracture networks based on the fracture shape, size, aperture, and distribution as well as the matrix permeability. Although this method does not consider the properties of the network, it is still widely used because of its simplicity. Even though it cannot accurately describe the flow process in the matrix in complex fracture networks, percolation theory still plays an important role in the calculations of the equivalent permeability [10]. In addition, the fractal properties of a fracture distribution introduced new ideas for

* Corresponding author.
E-mail address: tangchao@cdut.edu.cn (C. Tang).

calculations of the permeability [10]. A single continuum model is desirable due to its low level of modeling complexity and computational cost, but these benefits come at the cost of oversimplification.

To be more realistic, multi-continuum models have been developed, the most famous of which is the dual-porosity model. The underlying assumption of the multi-continuum approaches is that it is possible to represent different domains in the pore space, the dynamics within these domains, and the exchange between these domains based on continuous parameters and variables. The single-phase multi-continuum governing equations from the 1960s have been expanded to incorporate multi-phase flow [11–15], and they continue to be developed [16–18]. Since then, a dual-porosity model has been widely applied to the numerical simulations of fractured reservoirs. Currently, Kazemi's model is still the default option in most commercial software. In subsequent research, different improved models suitable for fractured media have been proposed. For example, Tecklenburg et al. [19] proposed a model to improve the dual-porosity model by simulating the effects of gravity, capillary infiltration, and other physical phenomena involved. This model was called the multiple interacting continua model (MINC). March et al. [20] presented a calculation method for the shape factor in the case of unsteady flow, compared it with the calculation results of a fine grid, and obtained consistent results. Implicit models are suitable in the case where a porous medium is regarded as a homogeneous medium and a fracture−matrix medium can be regarded as being composed of two parts: fractures and the matrix. In the case where fractures are less developed and their distribution is homogeneous, this kind of medium can be simulated by a representative elementary volume (REV) [21]. However, some scholars have suggested that as the number of fractures increases, the interactions between the fractures becomes stronger [22,23]. In addition, there is no clear scale separation between the pore scale, fracture widths, fracture lengths, and macroscale of interest [24]. Hence, the presence of fractures challenges the REV concept in fractured media modeling.

Therefore, explicit models of fractured reservoirs have been developed, the most representative of which is a discrete fracture model (DFM) [25,26]. In contrast with implicit models, explicit models preserve the fractures and matrix as separate geometric objects and make a geometric distinction between them. These models can accurately describe the fracture morphology and distribution and have significant advantages in terms of anisotropy and heterogeneity analysis. At the same time, to adapt to a complex fracture network generated by explicit models, a mesh generation technology has been developed. Moinfar et al. [27] introduced an unstructured PEBI (perpendicular bisector) mesh into a numerical reservoir simulation, and scaled up an unstructured Delaunay triangular mesh with a wavelet transform method to improve the calculation speed [28]. The development of unstructured meshes provides a basis for the high-accuracy and high-speed simulation of explicit fracture models.

The above conceptual models and their corresponding numerical discretization methods still have the following problems to be solved:

1) The existing implicit methods (based on single-continuum models and multi-continuum models) assume a continuum medium, and yet real fractures are defined as discontinuities in a medium. Many studies have made significant contributions to the further understanding of heterogeneous fracture distributions, but most of the improvements were based on modifying the type of statistical distribution function, which is usually only applicable to specific areas [29–31]. The extreme difference between the permeability of the fracture and the surrounding grid may cause the model equations to be unsolvable. At the same time, the extreme difference between the fracture aperture and the grid step makes it difficult to assign a value to the permeability of the grid. This implies that with an increase in the fracture heterogeneity and the cluster effect, continuum media theory will no longer be applicable.

2) For the explicit methods (discrete fracture matrix model (DFM) and discrete fracture network model (DFN)), if an equidimensional representation of the fractures is adopted, a fine grid is needed to resolve the fractures and avoid large aspect ratios of the fracture objects, which means that computational resources are wasted, and the underlying problem may even become unsolvable [32]. With a mixed-dimensional representation of a fractured medium introduced by a DFM [25,26] and an embedded discrete fracture method (EDFM) [33], the dimension of the fracture objects is one lower than that of the matrix objects, and this issue is avoided. However, a lower fracture dimension results in flow discontinuity and a saturation step at the fracture−matrix interfaces. As a result, an explicit model is inferior to an implicit model in terms of the computational stability and convergence.

Remaining challenges in the modeling and discretization of the flow in fractured porous media is the appropriate selection of the conceptual model (as illustrated in Table 1), the corresponding governing equations, and the necessary upscaling procedures and discretization approaches. In this research, a multi-scale discrete-fracture-network two-phase flow model was established based on a fractal distribution of implicit microfractures and the characteristic parameters of the explicit discrete large-scale fractures to analyze the effect of different scale fracture systems on the water saturation in a fractured reservoir during a waterflooding process. At the same time, the spatial discontinuity caused by the dimensionality reduction is corrected by introducing a dimensionless aperture factor. Furthermore, a solution scheme is redefined by a convection boundedness criterion [34], and the domain is discretized by the finite volume method to improve convergence and accuracy of the explicit model.

The paper begins by discussing the representation of static fractures in porous media in Section 2, while models for the flow are presented in Section 3. Discretization approaches are discussed in Section 4. In Section 5, the effects of different fracture scales are discussed, as are the research challenges that remain, before the paper concludes in Section 6.
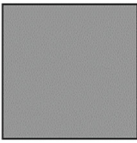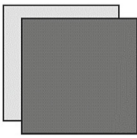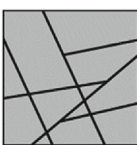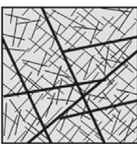
## 2. Static fracture model

### 2.1. Fracture location

In this work, the fractal characteristics of fracture networks are used to describe their heterogeneity. Tene et al. [35] presented a fractal model describing the pore size distribution in porous media. In this work, with similar theory, we present a fractal model that describes the fracture length distribution as follows:

$$n(l, L)dl = \alpha L^{D_c} l^{-(D_l+1)}, \tag{1}$$

$$N(L) = \frac{\alpha}{D_l} L^{D_c} l_{\min}^{-D_l}, \tag{2}$$

**Table 1**
Conceptual models of fractured porous media.

| Representation of fractures | Model | Conceptual illustration | Literature sources | Characteristics of Different Modeling |
|---|---|---|---|---|
| Implicit | Single-continuum model | | [29] [30] [31] | Suitable when fractures are weakly connected and small compared to the characteristic length scales of interest. However, failure to characterize the local geometry of the fracture network directly affects the flow patterns at the scale of interest. |
| | Multi-continuum model | | | |
| Explicit | Discrete fracture matrix model | | [25] [26] [32] [33] | Modeling within a framework with an explicit representation of fractures is often conceptually simpler than the implicit counterpart, but at the cost of dealing with complex geometries. |
| | Discrete fracture network model | | | |

where $n(l, L)$ is the number of fractures whose lengths are in the interval $[l, l+dl]$ in an $L \times L$ region, $D_c$ is the correlation dimension of the fracture location distribution, $D_l$ is the mass dimension of the fracture length distribution, $\alpha$ is the fracture density, $l_{min}$ is the shortest fracture length in the region, and $N(L)$ is the number of fractures with a length greater than $l_{min}$ in the region. In this work, two correlation functions are used to evaluate the probability that any two fractures belong to the same cluster when calculating $D_c$:

$$C(r) = \frac{2N_d(r)}{N(N-1)} \tag{3}$$

where $C(r)$ is the probability that two fractures with a centroid distance less than $r$ are in the same cluster, $N$ is the total number of fractures in the region, and $N_d(r)$ is the number of pairs of centers whose distance is less than $r$. By plotting $C(r)$ and $r$ on bi-logarithmic axes, the following scaling relationship can be determined: $C(r) \propto r^{D_c}$, where $D_c$ is the correlation dimension obtained by measuring the slope of this curve.

According to the definition of the correlation dimension, when the distance between the centroids of two fractures is less than $r$, these two fractures are likely to belong to the same fracture cluster. As shown in Fig. 1, with a change in the correlation dimension, cluster effects of different degrees appeared in the fracture network.

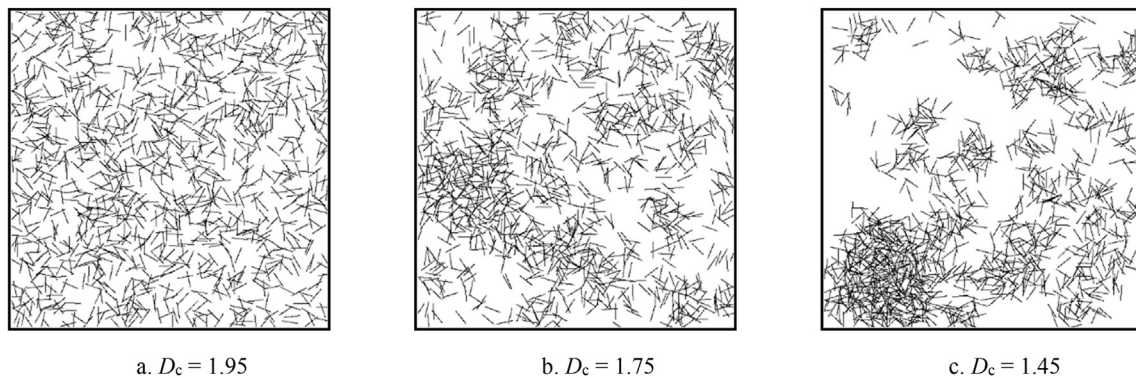A relatively simple method for the numerical simulation of



a. $D_c = 1.95$

b. $D_c = 1.75$

c. $D_c = 1.45$

**Fig. 1.** Contrast graphs of fracture networks with different correlation dimensions: a. $D_c = 1.95$, which is very close to the Euclidean dimension, so the fracture distribution is consistent with a uniform distribution, b. $D_c = 1.75$, which deviates slightly from the Euclidean dimension, and the generated fracture network has a local cluster effect, and c. $D_c = 1.45$, which deviates significantly from the Euclidean dimension, and a strong clustering effect appears in the fracture network (in all three cases, the same parameters were used for the fracture length, density, and orientation distribution).

fractured reservoirs is to use a Poisson stochastic process to generate the fracture positions [36]. However, the fractal dimension obtained with this approach is close to the Euclidean dimension of the system. Thus, it cannot effectively characterize the cluster effect of a fracture network (Fig. 1a). In an iterative process, weight coefficients are introduced into the domain based on a density function. This is a convenient way to generate heterogeneous fracture distributions. However, the interrelationship between fractures cannot be described because the iterative processes are independent of each other.

In this work, a multifractal process is used to generate fracture centroids. As shown in Fig. 2, the multifractal process is also an iterative method. Different from the Poisson process or a method considering weight coefficients, the multifractal process uses a multifractal spectrum to construct an internal relationship between different subdomains. Such probabilities $P_i$ of different subdomains are calculated as follows:

$$\sum_{i=1}^{n} \frac{P_i^q}{(1/sr)^{(q-1)D_q}} = 1. \tag{4}$$

Eq. (4) is commonly referred to as a multifractal spectrum, where $P_i$ is a probability, $sr$ is the scale ratio between the scales of the parent domain and the subdomain, and $D_q$ is a multifractal dimension. When $q = 0$, $D_q$ corresponds to a box-counting dimension; when $q = 1$, $D_q$ corresponds to an information dimension; when $q = 2$, $D_q$ corresponds to a correlation dimension. In this study, the correlation dimension was adopted to describe the relative locations of the fractures, so $q$ was fixed at 2.

The main advantage of a multifractal process is that it can simulate the cluster property of fractures. Under field conditions, fractures tend to form in clusters. Therefore, this property can be used to establish a more realistic static fracture network model.

## 2.2. Fracture orientation

The fracture orientation in a formation is determined by the load, stress field, geochemistry, and other factors at a local or regional scale. A probability distribution is a simple and widely used method to describe the fracture orientation. The most commonly used is the von Mises distribution [37], with the probability density distribution function and a cumulative probability distribution function defined respectively as follows:

$$f(\varphi|\mu,\kappa) = \frac{e^{\kappa \cos(\varphi-\mu)}}{2\pi I_0(\kappa)}, \tag{5}$$

$$F(\varphi|\mu,\kappa) = \frac{\int_0^{\varphi} e^{\kappa \cos(t-\mu)}dt}{2\pi I_0(\kappa)}, \tag{6}$$

where $\varphi$ is the fracture orientation, $\mu$ and $\kappa$ are the parameters describing the dominant orientation of the fracture distribution, and $I_0(\kappa)$ is a modified Bessel function, defined as $I_0(\kappa) = \sum_{i=0}^{+\infty} \frac{\kappa^{2i}}{2^{2i}(i!)^2}$. Since $\mu$ and $\kappa$ are difficult to obtain in field applications, the Fisher distribution [38] was adopted to generate the fracture orientation in this study. Its probability density distribution function can be expressed as

$$f(\theta) = \frac{K \sin\theta e^{K\cos\theta}}{e^K - e^{-K}} (0 < \theta < \pi/2), \tag{7}$$

where $\theta$ is an angular deviation from the mean, $K$ is Fisher's constant, which can be calculated by analyzing data, such as the surface outcrop data, to show the extent to which the fracture orientation deviates from the dominant orientation.
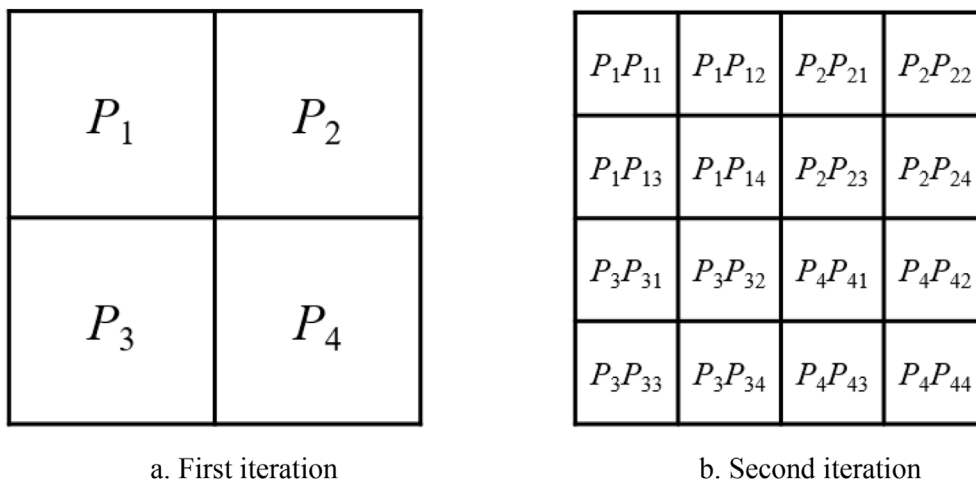


a. First iteration      b. Second iteration

**Fig. 2.** Schematic diagram of the iterative method for a multifractal process. a. First, the domain is divided into several subdomains until the number of subdomains reaches the required value, and then a probability $P_i$ is assigned to each subdomain randomly. b. In the next step, each subdomain is treated as a parent domain and divided into smaller subdomains. A new probability $P_i$ is re-randomly assigned and multiplied by the probability of the parent domain as the probability of the current subdomain.

## 3. Fracture flow model

### 3.1. Model hypotheses

As mentioned previously, due to the existence of scale effects, a fracture network in a real fractured reservoir is complex, which is mainly caused by changes in the in-situ stresses (extrusion and tensile) and the effect of environmental factors (leaching and dissolution). Once fractures are generated and extended, they will form channels for energy exchange within the reservoir, and the permeability of the reservoir will be significantly enhanced. If the matrix is treated as a uniform medium, the fractured medium can be considered to be a two-medium composite of the matrix and fractures. When a fracture distribution is uniform and its size is small, the dual-medium theory can be used to analyze the reservoir permeability. As local stress and environmental factors change over time, the fracture density will gradually increase and strengthen the interactions between fractures. Multi-scale fractures will begin to appear. At this time, the continuum theory is no longer applicable for the description of fractured reservoirs. In this study, the matrix and microfractures were established by using a dual-medium model, and large-scale fractures were established by using a discrete fracture model.

To simplify the model development, the following assumptions are made:

1) The flow is isothermal oil—water two-phase flow;
2) A Warren—Root model is used for the matrix—microfracture system, considering the dual-porosity/permeability;
3) The reservoir is simplified to a plane, where the depth is in the middle of the reservoir, and large-scale fractures are dimensionally reduced to one-dimensional linear elements;
4) The fluids are slightly compressible, and the reservoir rock is rigid.

### 3.2. Governing equations

From the law of mass conservation, the oil—water two-phase continuity equations can be written as

$$\frac{\partial(\rho_o \varphi s_o)}{\partial t} + \nabla \cdot (\rho_o \mathbf{v_o}) = 0, \tag{8}$$

$$\frac{\partial(\rho_w \varphi s_w)}{\partial t} + \nabla \cdot (\rho_w \mathbf{v_w}) = 0. \tag{9}$$

The water phase is assumed to be the wetting phase under the reservoir conditions. For immiscible two-phase flow, the supplementary equations are

$$\begin{aligned} s_o + s_w &= 1 \\ p_c &= p_o - p_w \end{aligned}. \tag{10}$$

In the formulas above, the oil and water densities are under formation conditions, which are generally unknown. Instead, they are expressed by the densities under standard conditions and formation volume factors. The crossflow between the matrix and microfractures is considered to be a pseudo-steady flow, that is, the rate of the crossflow is proportional to the pressure difference and inversely proportional to the fluid viscosities. The governing equations in the matrix and microfractures can be written as follows:

#### 3.2.1. Matrix system

$$\nabla \cdot \left[ \left( \frac{K_{rom}}{\mu_o B_o} \right) \nabla p_{om} \right] - \alpha \frac{p_{om} - p_{of}}{K_m \mu_o B_o} = \frac{1}{K_m B_o} \frac{\partial[\varphi_m(1 - s_{wm})]}{\partial t}, \tag{11}$$

$$\nabla \cdot \left[ \left( \frac{K_{rwm}}{\mu_w B_w} \right) \nabla (p_{om} - p_{cm}) \right. \\ \times \left. \right] - \alpha \cdot \frac{p_{om} - p_{cm} - p_{of} + p_{cf}}{K_m \mu_w B_w} = \frac{1}{K_m B_w} \frac{\partial(\varphi_m s_{wm})}{\partial t}. \tag{12}$$

#### 3.2.2. Microfracture system

$$\nabla \cdot \left[ \left( \frac{K_{rof}}{\mu_o B_o} \right) \nabla p_{of} \right] + \alpha \frac{p_{om} - p_{of}}{K_m \mu_o B_o} = \frac{1}{K_f B_o} \frac{\partial\left[\varphi_f\left(1 - s_{wf}\right)\right]}{\partial t}, \tag{13}$$

$$\nabla \cdot \left[ \left( \frac{K_{rwf}}{\mu_w B_w} \right) \nabla \left(p_{of} - p_{cf}\right) \right. \\ \times \left. \right] + \alpha \cdot \frac{p_{om} - p_{cm} - p_{of} + p_{cf}}{K_m \mu_w B_w} = \frac{1}{K_f B_w} \frac{\partial\left(\varphi_f s_{wf}\right)}{\partial t}. \tag{14}$$

#### 3.2.3. Large-scale fracture system

A mixed-dimensional representation is adopted to deal with large-scale fractures, which effectively avoids the problem of non-convergence caused by a large grid ratio. Since the large-scale fractures are represented by one-dimensional linear elements within a grid, the governing equations in these fractures can be expressed as

$$d_F \frac{\partial}{\partial l} \left( \frac{K_{roF}}{\mu_o B_o} \frac{\partial p_{oF}}{\partial l} \right) = d_F \frac{1}{K_F B_o} \frac{\partial[\varphi_F(1 - s_{wF})]}{\partial t}, \tag{15}$$

$$d_F \frac{\partial}{\partial l} \left[ \frac{K_{rwF}}{\mu_w B_w} \frac{\partial(p_{oF} - p_{cF})}{\partial l} \right] = d_F \frac{1}{K_F B_w} \frac{\partial(\varphi_F s_{wF})}{\partial t}. \tag{16}$$

The main problem with the mixed-dimensional strategy is the discontinuity of the flow due to the failure to describe large-scale fracture apertures. This is because, by definition [25], even a small amount of fluid flowing into the fractures from the inlet end can reach the outlet end in an instant. This results in flux discontinuities at fractures, although the model as a whole still obeys the conservation of mass. In this work, a dimensionless fracture aperture operator $d_F$ is introduced to avoid this problem. When $d_F$ is a constant, a smooth plate model with a certain aperture can be described; when $d_F$ is a specific function, a fracture surface with its corresponding roughness can be described.

Eqs. (11)–(16) are the saturation equations, and the corresponding pressure equations are obtained by eliminating the saturation terms. The mathematical model can be obtained as follows:

$$\nabla \cdot \left[ \left( \frac{K_{rom}}{\mu_o} + \frac{K_{rwm}}{\mu_w} \right) \nabla p_{om} \right] - \nabla \cdot \left( \frac{K_{rwm}}{\mu_w} \nabla p_{cm} \right) - \alpha \left( \frac{p_{om} - p_{of}}{K_m \mu_o} + \frac{p_{om} - p_{cm} - p_{of} + p_{cf}}{K_m \mu_w} \right) = 0. \tag{17}$$

$$\frac{1}{K_m} \frac{\partial (\varphi_m s_{wm})}{\partial t} - \nabla \cdot \left[ \left( \frac{K_{rwm}}{\mu_w} \right) \nabla (p_{om} - p_{cm}) \right] + \alpha \frac{p_{om} - p_{cm} - p_{of} + p_{cf}}{K_m \mu_w} = 0 \tag{18}$$

$$\nabla \cdot \left[ \left( \frac{K_{rof}}{\mu_o} + \frac{K_{rwf}}{\mu_w} \right) \nabla p_{of} \right] - \nabla \cdot \left( \frac{K_{rwf}}{\mu_w} \nabla p_{cf} \right) + \alpha \cdot \left( \frac{p_{om} - p_{of}}{K_m \mu_o} + \frac{p_{om} - p_{cm} - p_{of} + p_{cf}}{K_m \mu_w} \right) = 0 \tag{19}$$

$$\frac{1}{K_f} \frac{\partial (\varphi_f s_{wf})}{\partial t} - \nabla \cdot \left[ \left( \frac{K_{rwf}}{\mu_w} \right) \nabla (p_{of} - p_{cf}) \right] - \alpha \frac{p_{om} - p_{cm} - p_{of} + p_{cf}}{K_m \mu_w} = 0 \tag{20}$$

$$d_F \frac{\partial}{\partial l} \left[ \left( \frac{K_{roF}}{\mu_o} + \frac{K_{rwF}}{\mu_w} \right) \frac{\partial p_{oF}}{\partial l} \right] - d_F \frac{\partial}{\partial l} \left( \frac{K_{rwF}}{\mu_w} \frac{\partial p_{cF}}{\partial l} \right) = 0 \tag{21}$$

$$d_F \frac{1}{K_F} \frac{\partial (\varphi_F s_{wF})}{\partial t} - d_F \frac{\partial}{\partial l} \left[ \frac{K_{rwF}}{\mu_w} \frac{\partial (p_{oF} - p_{cF})}{\partial l} \right] = 0 \tag{22}$$

A crossflow term is missing from the large-scale fracture governing equations. Relevant studies have confirmed that the flow through an interface of each medium is continuous. As a result, the cross fluxes between the matrix–microfracture system and the large-scale fracture system will cancel each other in the process of flow equation superposition [39]. The above equations are not closed, so it is necessary to construct an auxiliary equation. Riquelme et al. [40] used the following relationship between the capillary pressure and water saturation:

$$p_{ci} = -\beta_i \ln(s_{wi}). \tag{23}$$

Eq. (23) implies that the capillary pressure at an interface of different media should be continuous. Based on this continuity condition, a water saturation function relationship between the micro-fracture system and the large-scale fracture system can be established at the interface:

$$p_{cf}\left( s_{wf} \right) = p_{cF}(s_{wF}). \tag{24}$$

The inverse function of the water saturation in micro-fractures can be used to represent the water saturation in large scale fractures:

$$s_{wF} = (p_{cF})^{-1} p_{cf}\left( s_{wf} \right). \tag{25}$$

Based on the chain rule, the water-phase saturation equation (22) in large-scale fractures can be rewritten by using the water saturation of the microfractures, which can be expressed as follows:

$$d_F \frac{1}{K_F} \frac{ds_{wF}}{ds_{wf}} \frac{\partial (\varphi_F s_{wf})}{\partial t} - d_F \frac{\partial}{\partial l} \left[ \lambda_{wF} \frac{\partial (p_{oF} - p_{cF})}{\partial l} \right] = 0. \tag{26}$$

### 3.3. Initial conditions

In the initial state, the pressure at each point in the formation is equal to the original formation pressure, and the water saturation at each point is equal to the irreducible water saturation, so the model has the following initial conditions:

$$p_m(x,y,z,t)|_{t=0} = p_f(x,y,z,t)\Big|_{t=0} = p_F(x,y,z,t)|_{t=0} = p_i$$
$$s_{wm}(x,y,z,t)|_{t=0} = s_{wf}(x,y,z,t)\Big|_{t=0} = s_{wF}(x,y,z,t)|_{t=0} = s_{wc}. \tag{27}$$

### 3.4. External boundary conditions

$\Gamma_{out}$ represents the reservoir boundary, and the outer boundary of the model is assumed to be closed. Thus, the model has the following outer boundary conditions:

$$\frac{\partial p}{\partial n}\Big|_{\Gamma_{out}} = 0. \tag{28}$$

### 3.5. Well model

A common approach to model wells is Peaceman's approach [41], which turns a well into a point source or sink and calculates the flux by calculating the equivalent radius of the well and then replacing its bottom hole pressure with a grid pressure.

In this work, a wellbore is reduced to a one-dimensional linear entity as an internal boundary condition, and its flux is calculated by a bottom hole pressure gradient. This method avoids the problem of mesh discretization caused by the wellbore size.

Based on radial unsteady flow in a plane, a flux at each wellbore boundary can be obtained by giving a bottom hole pressure gradient. $\Gamma_{well}$ represents the wellbore boundary. The constant flow production is imposed by the following boundary condition in actual field applications:

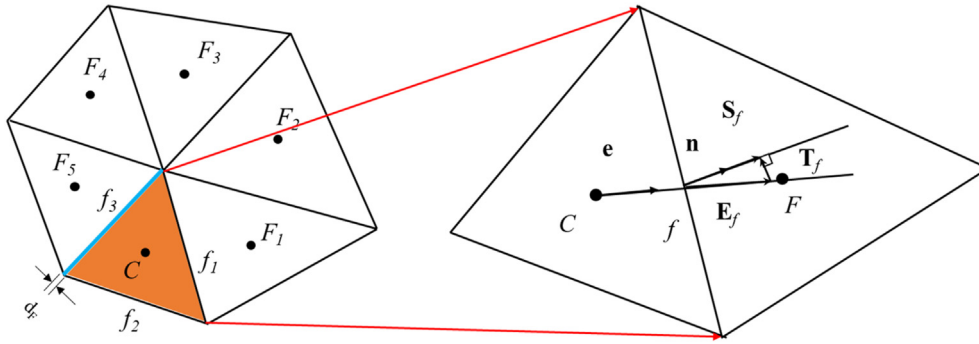$$\frac{\partial p}{\partial n}\Big|_{\Gamma_{well}} = -\frac{\mu Q}{2\pi K h r_w}. \tag{29}$$

**Fig. 3.** Selection of control elements and the distribution of adjacent geometric entities. The matrix and micro-fracture systems are expressed as a triangular grid, considered as a dual-continuous medium. The one-dimensional blue line is decomposed in triangular elements that are bounds of the triangles surrounding a large-scale fracture. $\mathbf{e}$ is the unit vector along the direction defined by a vector $\mathbf{CF}$, $\mathbf{S}_f$ is the surface vector, which can be written as the sum of two vectors $\mathbf{E}_f$ and $\mathbf{T}_f$ ($\mathbf{E}_f$ is in the CF direction, $\mathbf{T}_f$ is perpendicular to the unit normal vector $\mathbf{n}$). (For interpretation of the references to colour in this figure legend, the reader is referred to the Web version of this article.)

When the oil yield is fixed, the water yield is calculated by a two-phase fluidity ratio. When the liquid yield is fixed, the water content is determined according to the two-phase fluidity, and the oil and water yields can be distributed based on the water content.

## 4. Discretization and numerical solutions

### 4.1. Domain discretization

According to the above hypotheses, a reservoir is divided into a matrix, microfractures, and large-scale fractures. The matrix and micro-fractures can be considered to be dual media, and large-scale fractures can be considered to be a discrete medium to realize the physical modeling of the multi-media with multi-scale fractures.

The whole computational domain is discretized by unstructured Delaunay triangles. Large-scale fractures are dimensionally reduced as the inner boundaries of the model, which are represented by the interfaces of one-dimensional line elements between the triangular grids. Based on the finite volume method, a control element is determined by triangles, and their boundaries generated by the discretization [42]. This method ensures that the control elements do not overlap and cover the entire computational domain. The computational domain ($\Gamma_d$) consists of two sub-domains: the matrix−microfracture system ($\Gamma_{m-f}$) and the large-scale fracture system ($\Gamma_F$).FGE represents the flow governing equations. The integration of the whole computational domain can be written as

$$\iiint_{\Gamma_d}(\text{FGE})\,d\Gamma_d = \iiint_{\Gamma_{m-f}}(\text{FGE})\,d\Gamma_{m-f} + d_F \times \iiint_{\Gamma_F}(\text{FGE})\,d\Gamma_F. \qquad (30)$$

### 4.2. Equation discretization

The result of the domain discretization is that the whole computational domain is divided into non-overlapping control elements. As shown in Fig. 3, to obtain the algebraic equations, the flow governing equations need to be discretized in the control elements based on the finite volume method. These equations in the matrix are taken as an example; a similar process is carried out for the microfractures and large-scale fractures.

The process starts by integrating Eq. (18) over a control element $C$:

$$\int_{V_C}\frac{\partial(\varphi s_w)}{\partial t}\,dV - \int_{V_C}\nabla\cdot[\lambda_w\nabla(p_o - p_c)]\,dV + \int_{V_C}q_w\,dV = 0. \qquad (31)$$

According to the volume integral property, Eq. (31) shows that the flow process described in Eq. (18) still obeys the law of mass conservation in any non-zero volume grid. Compared with the finite element method, this feature is a huge advantage of the finite volume method, because it mathematically guarantees that mass is conserved in any local grid.

The first item in Eq. (31) can be expressed by referring to Eq. (30) as follows:

$$\int_{V_C}\frac{\partial(\varphi s_w)}{\partial t}\,dV = V_C\varphi_m\frac{ds_{wm}}{ds_{wf}}\frac{\partial s_{wf}}{\partial t} + V_C\varphi_f\frac{\partial s_{wf}}{\partial t}$$

$$+ \sum_{f\sim faces(V_C-F)}\frac{ds_{wF}}{ds_{wf}}\frac{\partial s_{wf}}{\partial t}d_F l_F\varphi_F. \qquad (32)$$

The first term on the right-hand side is the variation rate of the water phase saturation in a pore volume in the matrix in the control element $V_C$, the second term is the variation rate of the water phase saturation in a micro-fracture pore volume, and the third term is the variation rate of the water phase saturation in a large-scale-fracture pore volume at the boundary surface $f$ of the control element.

According to the divergence theorem, the volume integral in the advection term in Eq. (31) can be converted into a surface integral, as follows:

$$\int_{V_C}\frac{\partial(\varphi s_w)}{\partial t}\,dV - \oint_{\partial V_C}[\lambda_w\nabla(p_o - p_c)\cdot\boldsymbol{n}]\,dS + \int_{V_C}q_w\,dV = 0. \qquad (33)$$

Furthermore, the surface integral is written in the form of the sum of the surface integrals of each surface of the control element:

$$\oint_{\partial V_C}[\lambda_w\nabla(p_o - p_c)\cdot\boldsymbol{n}]\,dS = \sum_{f\sim faces(V_C)}\left(\int_f[\lambda_w\nabla(p_o - p_c)\cdot\boldsymbol{n}]\,dS\right). \qquad (34)$$

Using a one-point Gaussian quadrature, the integral at the face $f$ of the element becomes

[43] (i.e., the influence of the flow direction is considered). Because the first-order upwind scheme produces severe false diffusion

$$\oint_{\partial V_C} [\lambda_w \nabla(p_o - p_c) \cdot \boldsymbol{n}] dS \approx \sum_{f \sim faces(V_C)} \left[ \lambda_{wm}(s_{wm}^{up}) \nabla(p_{om} - p_{cm}) + \lambda_{wf}(s_{wf}^{up}) \nabla(p_{of} - p_{cf}) \right] \cdot \boldsymbol{S}_f + \sum_{f \sim faces(V_C - F)} d_F \lambda_{wF}(s_{wF}^{up}) \frac{\partial(p_{oF} - p_{cF})}{\partial l}. \quad (36)$$

$$\int_f [\lambda_w \nabla(p_o - p_c) \cdot \boldsymbol{n}] dS = \lambda_w \nabla(p_o - p_c) \cdot \boldsymbol{S}_f. \quad (35)$$

Similarly, according to the form of Eq. (30), the advection term in Eq. (31) can be rewritten as

The first term on the right-hand side represents the flux through the boundary of the matrix−microfracture system, and the second term represents the flux through the large-scale fractures. The

(called cross-stream diffusion or numerical diffusion in the literature), the numerical solution deviates greatly from the true solution, so a high-order upwind scheme is adopted. However, due to the large difference between the large-scale fractures and matrix−microfractures in terms of conductivity, the high-order upwind scheme will generate non-physical oscillations at an interface between the matrix−microfracture system and the large-scale fracture system. In addition, dimensionality reduction of the

$$\left( V_C \varphi_m \frac{ds_{wm}}{ds_{wf}} + V_C \varphi_f + \sum_{f \sim faces(V_C - F)} \frac{ds_{wF}}{ds_{wf}} d_F l_F \varphi_F \right) \frac{\partial s_{wf}}{\partial t} - \left\{ \sum_{f \sim faces(V_C)} \left[ \lambda_{wm}(s_{wm}^{up}) \nabla(p_{om} - p_{cm}) + \lambda_{wf}(s_{wf}^{up}) \nabla(p_{of} - p_{cf}) \right] \cdot \boldsymbol{S}_f + \right.$$
$$+ \quad . \qquad \left. \sum_{f \sim faces(V_C - F)} d_F \lambda_{wF}(s_{wF}^{up}) \frac{\partial(p_{oF} - p_{cF})}{\partial l} \right\} + \left( q_{wm} V_C + q_{wf} V_C + \sum_{f \sim faces(V_C - F)} d_F l_F q_{wF} \right) = 0 \quad (38)$$

superscript represents upstream weighting.

The integral of the source and sink terms in Eq. (31) can be approximately written as

large-scale fractures is carried out in this work, resulting in more significant step phenomena at the interfaces. To overcome these problems, a modified higher-order upwind scheme for the saturation and flow is established by using the convection boundedness

$$\left[ \sum_{f \sim faces(V_C)} \left[ (\lambda_m + \lambda_f) \nabla p_o - \lambda_{wm} \nabla p_{cm} - \lambda_{wf} \nabla p_{cf} \right] \cdot \boldsymbol{S}_f + \sum_{f \sim faces(V_C - F)} d_F \left( \lambda_F \frac{\partial p_o}{\partial l} - \lambda_{wF} \frac{\partial p_{cF}}{\partial l} \right) \right] - \left[ (q_m + q_f) V_C + \sum_{f \sim faces(V_C - F)} d_F l_F q_F \right] = 0. \quad (39)$$

$$\int_{V_C} q_w dV \approx q_{wm} V_C + q_{wf} V_C + \sum_{f \sim faces(V_C - F)} d_F l_F q_{wF}. \quad (37)$$

Finally, for the control element $V_C$, the semi-discrete format of the saturation equation represented by Eq. (31) can be expressed as follows:

The above discretization process is also applicable to the pressure equation. Since the pressure is assumed to be continuous and no subscript representing a medium is added, the semi-discrete form of the pressure equation can be written as

criterion (CBC) [44].

As shown in Fig. 4, in the higher-order upwind scheme, the value $\Phi_f$ at the interface $f$ is determined by the upwind ($\Phi_C$), downwind ($\Phi_D$), and far upwind ($\Phi_U$) nodal values. The position of each point is determined by the flow direction. Thus, the value $\Phi_f$ can be expressed as follows:

$$\Phi_f = F(\Phi_U, \Phi_C, \Phi_D). \quad (40)$$

A new function $\tilde{\Phi}(x)$ is defined as follows:

$$\tilde{\Phi}(x) = \frac{\Phi_x - \Phi_U}{\Phi_D - \Phi_U}. \quad (41)$$

Eq. (40) can be rewritten with only one variable as

### 4.3. Modified higher-order upwind scheme

To avoid nonphysical solutions, the interpolation calculations of the saturation and fluidity are carried out with an upwind scheme

$$\tilde{\Phi}_f = G(\tilde{\Phi}_C). \quad (42)$$

According to the CBC, for a scheme to have the boundedness property, it should meet the following conditions:
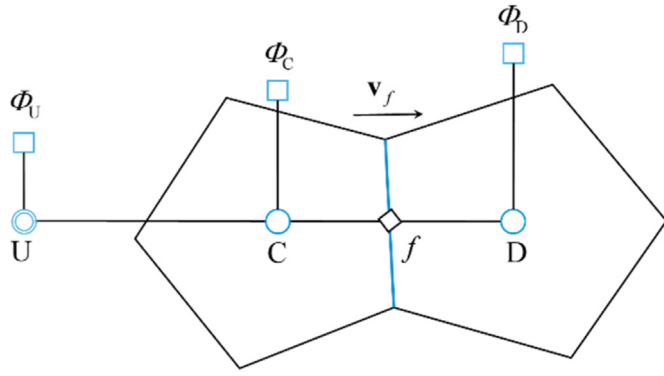
**Fig. 4.** Schematic of the upwind, downwind, and far upwind node locations used in describing the convection schemes in an unstructured grid.

1) Its functional relationship should be continuous;
2) It should be bounded from below by $\tilde{\Phi}_C$ and from above by unity;
3) It should pass through points (0,0) and (1,1) monotonically $(0 < \tilde{\Phi}_C < 1)$;
4) For $\tilde{\Phi}_C < 0$ or $\tilde{\Phi}_C > 1$, the functional relationship $G(\tilde{\Phi}_C)$ should be equal to $\tilde{\Phi}_C$.

A higher-order upwind scheme (such as the Quadratic Upstream Interpolation for Convective Kinematics (QUICK) scheme) is modified according to the CBC, and the corresponding function is established. The higher-order upwind scheme with the boundedness property can be constructed as follows:

$$\tilde{\Phi}_f = \begin{cases} 3\tilde{\Phi}_C & 0 \le \tilde{\Phi}_C \le \dfrac{1}{6} \\ \dfrac{3}{4}\tilde{\Phi}_C + \dfrac{3}{8}, & \dfrac{1}{6} \le \tilde{\Phi}_C \le \dfrac{7}{10} \\ \dfrac{1}{3}\tilde{\Phi}_C + \dfrac{2}{3}, & \dfrac{7}{10} \le \tilde{\Phi}_C \le 1 \\ \tilde{\Phi}_C, & \tilde{\Phi}_C > 1, \tilde{\Phi}_C < 0 \end{cases} \tag{43}$$

As shown in Fig. 5, compared with the exact solution, the saturation profile generated by the first-order upwind scheme is smeared and highly inaccurate but very smooth. This inaccuracy is due to false diffusion, which is caused by the one-dimensional interpolation profile used. This error can be reduced by using higher-order interpolation schemes, as demonstrated by the profile generated with the QUICK scheme. The QUICK scheme profile is shown to be much sharper and more accurate than the upwind profile. However, it suffers from over/undershoots near the sharp gradient. This error is called the dispersion error, which causes the generation of maxima/minima in the solution domain and is a characteristic of all higher-order (HO) schemes. The profile generated by the modified higher-order upwind scheme will limit the unphysical oscillations at the interface, which provides a more reasonable solution.

### 4.4. Iterative implicit pressure and explicit saturation (IMPES) solution

The saturation and pressure equations are solved by the implicit pressure and explicit saturation (IMPES) method. First, the pressure equation is computed implicitly, and then the saturation equation is evaluated explicitly. Assuming that the current time step is $k$, all
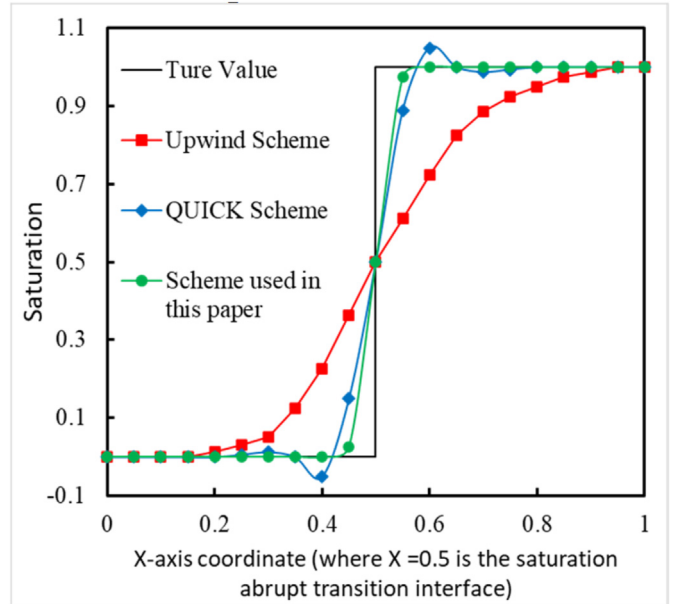


**Fig. 5.** Comparison of the solutions from different saturation profiles at an abrupt interface.

pressure-related variables are computed implicitly using the value at the $(k+1)$th time step, and then Eq. (31) can be written as

$$\sum_{f \sim faces(V_C)} \left[ \left( \lambda_m^k + \lambda_f^k \right) \nabla p_o^{k+1} \right]_f \cdot \boldsymbol{S}_f + \sum_{f \sim faces(V_C-F)} d_F \lambda_F^k \frac{\partial p_o^{k+1}}{\partial l}$$
$$= \sum_{f \sim faces(V_C)} \left( \lambda_{wm}^k \nabla p_{cm}^k + \lambda_{wf}^k \nabla p_{cf}^k \right)_f \cdot \boldsymbol{S}_f + \sum_{f \sim faces(V_C-F)} d_F \lambda_{wF}^k \frac{\partial p_{cF}^k}{\partial l} + .$$
$$\left[ \left( q_m + q_f \right) V_C + \sum_{f \sim faces(V_C-F)} d_F l_f q_F \right] \tag{44}$$

It should be noted that the capillary pressure in Eq. (44) uses the value of the $k$th time step, which is already known. Therefore, Eq. (44) only contains one unknown variable $p_o^{k+1}$, which can be solved by the Newton–Raphson iterative method. By substituting the results into the water saturation equation, $s_{wf}^{k+1}$ can be computed explicitly, as follows:

$$\left( V_C \varphi_m \frac{ds_{wm}}{ds_{wf}} + V_C \varphi_f + \sum_{f \sim faces(V_C-F)} \frac{ds_{wF}}{ds_{wf}} d_F l_f \varphi_F \right) \frac{s_{wf}^{k+1} - s_{wf}^k}{\Delta t}$$
$$= \left\{ \sum_{f \sim faces(V_C)} \left[ \lambda_{wm}^k \nabla \left( p_o^{k+1} - p_{cm}^k \right) + \lambda_{wf}^k \nabla \left( p_o^{k+1} - p_{cf}^k \right) \right] \cdot \boldsymbol{S}_f + . \right.$$
$$\left. \sum_{f \sim faces(V_C-F)} d_F \lambda_{wF}^k \frac{\partial \left( p_o^{k+1} - p_{cF}^k \right)}{\partial l} \right\} - \left( q_{wm} V_C + q_{wf} V_C \right.$$
$$+ \sum_{f \sim faces(V_C-F)} d_F l_f q_{wF} \bigg) \tag{45}$$

Since the variables related to the saturation are evaluated explicitly, each time step should not be too long, that is, the flow through the control element within each time step should not exceed the pore volume of the control element; otherwise, the IMPES method will have stability problems. The specific time step

selection criteria used in this work was presented by Chen et al. [43,45−47].

## 5. Numerical model for water flooding in multi-scale fractured reservoir

The size of the multi-scale fracture model established in this paper was 100 m × 100 m. The study area was divided into 8307 grid blocks by a Delaunay triangulation. The maximum grid side length was 7.5 m, and the minimum grid side length was 0.03 m. The grid quality was evaluated by the ratio of the grid block area to the radius of its circumscribed circle (the minimum was 0.65 and the average was 0.95, indicating that the gridding result met the simulation requirements). A specific grid shape and a large-scale fracture distribution are shown in Fig. 6. An injection well was located in the lower-left corner of the model, and a production well was located in the upper-right corner of the model. The wells and large-scale fractures were treated by a grid mesh encryption to enhance the stability of the calculations.

Compared with conventional commercial software model, the main advantages of the model established in this paper are as follows:

1) The whole study area was divided by Delaunay triangular grid segmentation, which significantly improved the adaptability of the irregular boundaries (inflection points and intersections of fractures);
2) Large-scale fractures were reduced by dimensionality reduction to the inner boundary of the model, effectively avoiding the computational cost brought by a minimization grid;
3) By introducing the dimensionless aperture of large-scale fractures, the problem of discontinuity of the large-scale fracture flow was solved, and the obtained results were more in line with real systems;
4) The higher-order upwind scheme was improved, and the improvement of the accuracy of the solution significantly suppressed the occurrence of non-physical oscillations.

### 5.1. Model validation

Since there is no commercial software to effectively simulate a multi-scale fracture system, to validate the above model, the large-scale fracture sub-model and the microfracture−matrix sub-model were validated by the analytical solution of the Buckledy−Leverett model and the numerical solution of a dual-medium model, respectively.

#### 5.1.1. Case I: large-scale fracture sub-model (compared to the Buckledy−Leverett model)
The large-scale fracture sub-model was first used to solve a one-dimensional flow process neglecting the capillary forces and gravity, namely the Buckledy−Leverett equation. The source and sink items were assumed to only appear at both ends of the one-dimensional reservoir, water was injected from the left side at a constant flow rate $q_w$, and the production was at the right side with a constant liquid yield $q_L$. The effective water saturation is defined as

$$s_e = (s_w - s_{wc}) / (1 - s_{wc} - s_{or}). \tag{46}$$

The relative permeabilities of the water and oil phases are denoted respectively as

$$K_{rw} = s_e^4, \tag{47}$$

$$K_{ro} = (1 - s_e)^2 \left(1 - s_e^2\right). \tag{48}$$

The relative permeability curves are shown in Fig. 7. The analytical solution of the Buckledy−Leverett equation can be expressed as

$$x(s_w, t) = x(s_w, 0) + \frac{f'(s_w)}{A\varphi} \int_0^t q_L \mathrm{d}t. \tag{49}$$

The values of the parameters used in the models are shown in Table 2. As shown in Fig. 8, the results of the analytical and numerical solutions for the large-scale fracture sub-model agreed closely.

#### 5.1.2. Case II: Microfracture and matrix system sub-model (compared with eclipse commercial software)
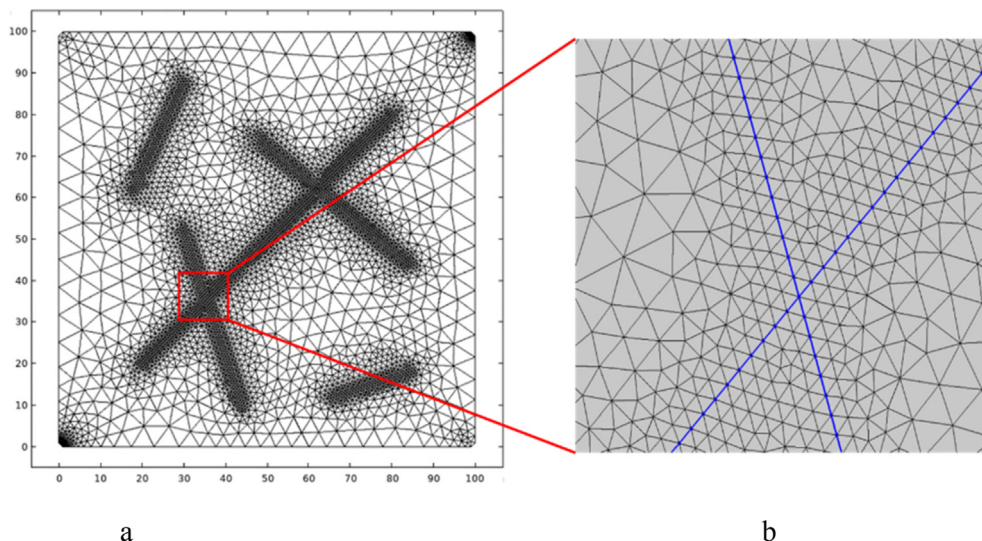A dual-medium model with dimensions of



**Fig. 6.** Results of grid subdivision of multiscale fractures: a. overall subdivision effect of the model and b. local reinforcement effect at large scale fractures.
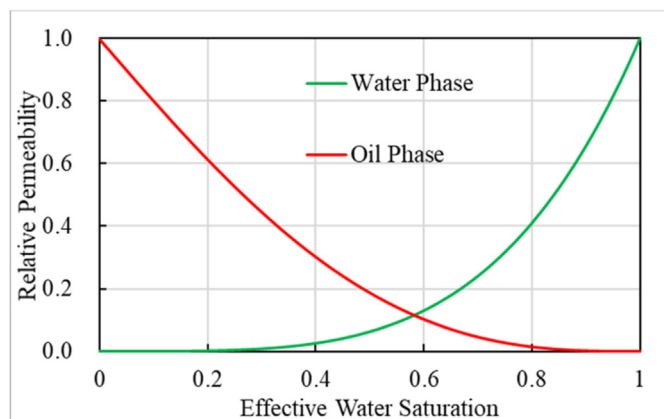
**Fig. 7.** Oil−water two-phase relative permeability curves in the matrix−microfracture system.



**Fig. 8.** Comparison between numerical and analytical solutions for the Buckledy−Leverett equation.

**Table 2**
Parameters used in the Buckledy−Leverett model.

| Parameter | Value |
|---|---|
| Fracture Length (m) | 100 |
| Fracture Permeability (mD) | 1500 |
| Reservoir Pressure (MPa) | 25 |
| Irreducible Water Saturation | 0 |
| Residual Oil Saturation | 0 |
| Water Phase Viscosity (mPa·s) | 1 |
| Oil Phase Viscosity (mPa·s) | 5 |
| Rate of Water Injection (m·s$^{-1}$) | $1 \times 10^{-5}$ |

**Table 3**
Parameters used in the dual-porosity model.

| Parameter | Value |
|---|---|
| Microfracture Permeability (mD) | 100 |
| Matrix Permeability (mD) | 10 |
| Formation Pressure (MPa) | 25 |
| Irreducible Water Saturation (decimal) | 0 |
| Residual Oil Saturation (decimal) | 0 |
| Water Phase Viscosity (mPa·s) | 1 |
| Oil Phase Viscosity (mPa·s) | 5 |
| Water Injection/Liquid Production (m$^3$/d) | 15 |
| Matrix Porosity (decimal) | 0.25 |
| Microfracture Porosity (decimal) | 0.3 |

100 m × 100 m × 10 m was established using the Eclipse reservoir numerical simulation software with a grid step size of 5 m × 5 m × 5 m. The crude oil was saturated in the initial state of the formation, and both the irreducible water and residual oil saturation were zero.

Gravity and the capillary forces were neglected, and the model was assumed to be isotropic. The lower-left corner of the model at (0,0) was the injection well, and the upper-right corner at (100 m, 100 m) was the production well. The other parameters are shown in Table 3. Fig. 9 shows the water saturation distributions from the model proposed in this paper and the Eclipse software at different times. The two predictions had good agreement.

### 5.2. Analysis of results and comparison of examples

#### 5.2.1. Effect of microfracture network on water saturation distribution

In the model validation process, it was assumed that both the matrix and microfractures were homogeneous, while the microfractures in an actual formation are not uniformly distributed. To describe the heterogeneity of microfractures and to study the effect of microfracture networks with a clustering effect on the water saturation in the water-flooding process in a fractured reservoir, the multiple fractal modeling method mentioned above was used to establish a fracture network with the clustering effect.

First, static modeling parameters were obtained through real seismic interpretation data. At present, the main method of using seismic data to characterize a fracture distribution is based on a post-stack seismic attribute data analysis, which is mostly used for the characterization and prediction of large-scale fractures but has a poor characterization of microfractures. Therefore, the ant tracking method proposed by the Schlumberger company was adopted in this paper. By combining image processing technology
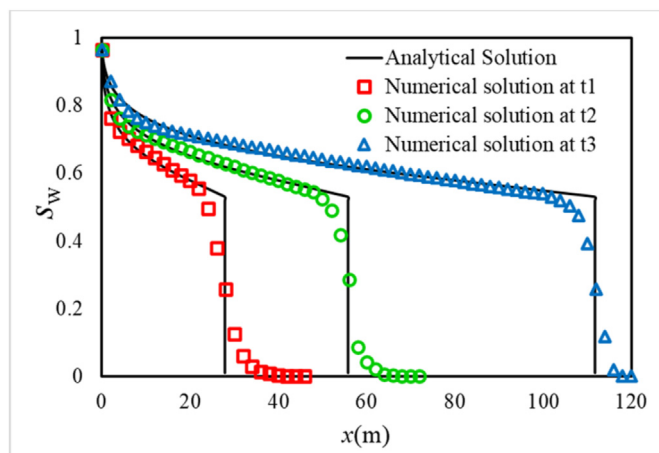
with three-dimensional seismic data, the characterization accuracy of post-stack seismic attribute data for the microfractures was effectively improved.

This procedure consisted of four steps. The first step was to condition the seismic data by reducing noise in the signal. The second step enhanced the spatial discontinuities in the seismic data (via fracture attribute generation and edge detection). The third step, which generated the Ant tracking volume, significantly improved the fracture attributes by suppressing the noise and remains of nonfracturing events. This was achieved by emulating the behavior of ant colonies in nature and how they use foramens to mark their paths to optimize the search for food. In this work, "artificial ants" were placed as seeds on a seismic discontinuity volume to search for fracture zones. Virtual pheromones deployed by the ants captured information related to the fracture zones in the volume. Through dynamic and static interwell connectivity analysis, the final stopping criterion is determined. The result was an attribute volume that showed the fracture zones very sharply and in detail.

Fig. 10 shows the results for the ant tracking of different strata reference depths in a certain block. The images intuitively show that there were microfractures with local cluster effects in the study area. The static model could be constrained with as much real stratigraphic data as possible to better ensure the consistency between the static modeling results and the real stratigraphic situation. After this, the slice of the corresponding depth was selected to generate a grayscale image to calculate the fracture correlation dimension. Therefore, the correlation dimension of the fracture network at different depths in the stratum was calculated by using Eq. (3), and the results are shown in Fig. 11.
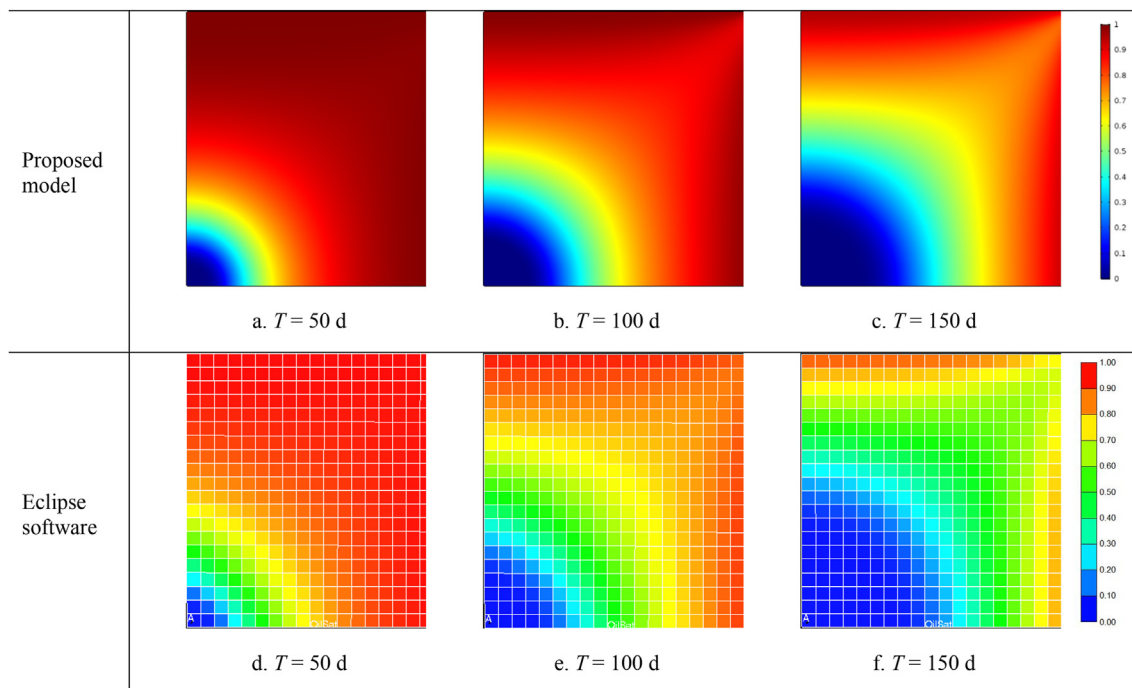
**Fig. 9.** Comparison of water saturation distributions between the model established in this paper and the Eclipse software model at different times.
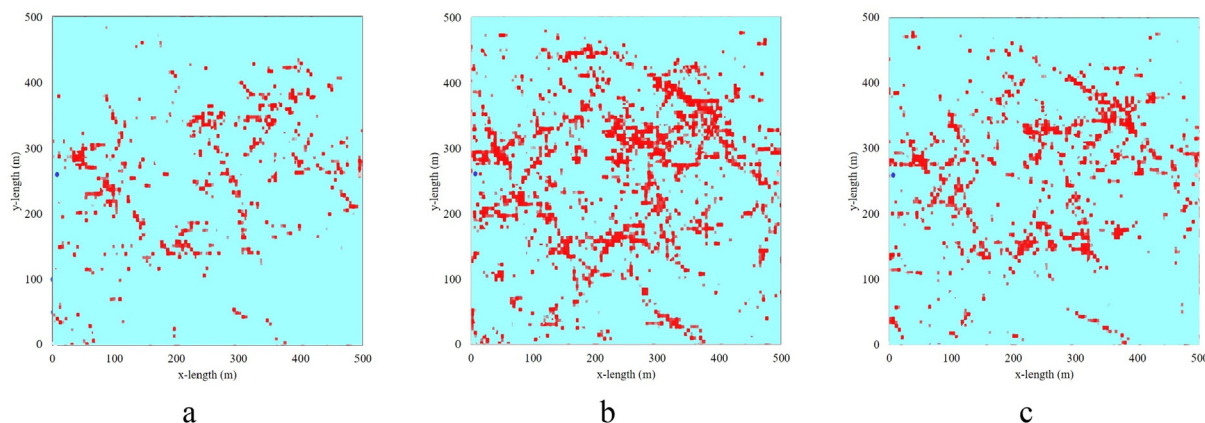


**Fig. 10.** Fracture images identified by seismic attribute volume data at different buried depth planes in an oil field block: a. buried depth = 6500 m, b. buried depth = 6510 m, and c. buried depth = 6520 m

According to the calculations, the correlation dimension of the microfracture network in the study area was about 1.75. To simplify the problem, it was assumed that the microfracture direction obeyed a uniform distribution, and a fixed-length model was used to generate a fracture network pattern with the fractal features of a real fracture network pattern (Fig. 12).

Fig. 13 shows the absolute permeability distribution of the matrix and microfracture system of the model. Using the same model parameters as in case I, the distribution diagram of the water saturation at different water injection times were obtained, and the results are shown in Fig. 14.

The numerical simulation results showed that a non-uniform distribution of the microfractures increased the irregularity of the oil−water front morphology. The cluster effect of the selected microfracture network was not strong ($D_c$ = 1.75), and thus, the microfracture network showed no evident cutting effect on the oil−water front morphology in this case. The other parameters of

the model were kept unchanged, and the matrix−microfracture dual-medium model with a microfracture correlation dimension of 1.45 was established for the numerical simulations. The results are shown in Fig. 15.

The above results indicated that the heterogeneity of the reservoir will complicate the oil−water front distribution, and the cluster effect of the microfracture network will further aggravate the complexity of the oil−water front shape. The local cluster areas of the microfractures should be given sufficient attention, and the corresponding well pattern and drilling method should be adopted based on the distribution of fractures.

### 5.2.2. Effect of large-scale fracture network on water saturation distribution

To clarify the main controlling factors of the water injection development dynamics in multi-scale fractured reservoirs, numerical simulations of large-scale fractures were carried out based
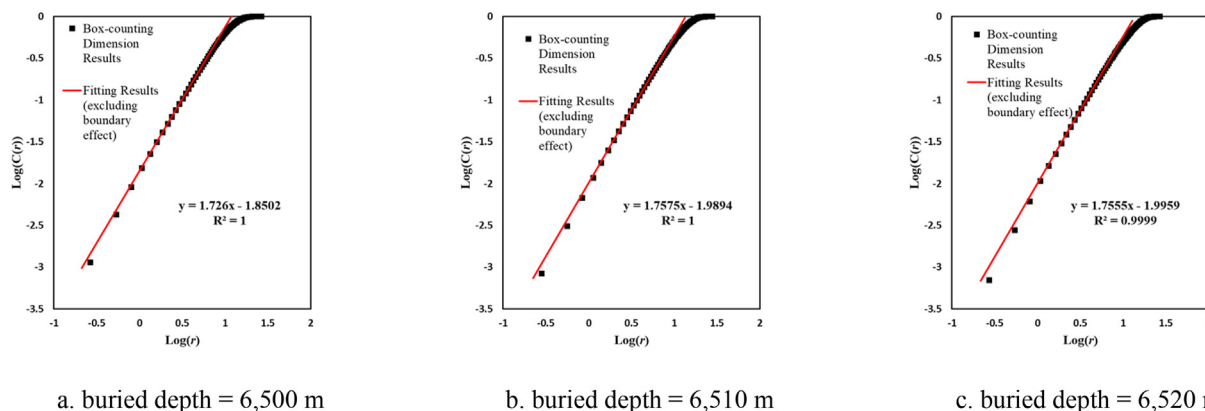
a. buried depth = 6,500 m          b. buried depth = 6,510 m          c. buried depth = 6,520 m

**Fig. 11.** Fractal correlation dimension calculations and fitting results of fracture images at different buried depths.
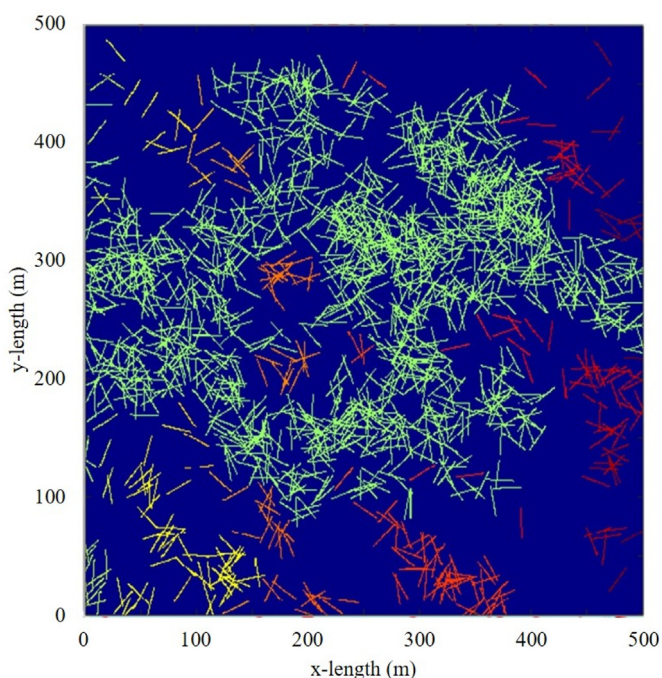


**Fig. 12.** Microfracture network generated by a multifractal method. By staining, the connectivity of different fractures is revealed. Due to the non-uniform distribution of fractures, disconnected fracture clusters formed locally (red/yellow/orange clusters), and there was no direct connection between them and the main percolation cluster (green clusters).

on the model described above. Since the conductivity of large-scale fractures is significantly different from that of the microfractures, different relative permeability curves should be used. According to Aguilera's research [1], when the fracture conductivity is large enough, the influence of the capillary pressure on the multiphase flow can be neglected. In this case, the relative permeability curves shown in Fig. 16 can be used. The results are shown in Fig. 17.

The numerical simulation results showed that compared with a microfracture network, the large-scale fractures had more significant effects on the waterflood front shape, and thus, it is necessary to analyze the influence of the large-scale fracture morphology on the water saturation distribution. To clarify the influence of large-scale fractures on the saturation distribution and the production

process, it is first necessary to eliminate the influence of the non-uniform distribution of microfractures on the results. It is assumed that the directions and locations of the microfractures followed uniform distributions.

The matrix−microfracture system was equivalently treated as a dual-medium model, and a large-scale fracture with a length of 90 m and an aperture of 0.5 mm was additionally constructed. The absolute permeability was calculated by a cubic function. The connection direction of the injection-production wells was the reference direction, and the production of the wells was calculated when the angle between the large-scale fracture and the reference direction was 0°, 45°, and 90°. The results are shown in Fig. 18.

The analysis of the calculated results in Fig. 19 showed that the smaller the angle between the fracture and the direction of the mainstream line was, the earlier the water breakthrough of the production well was, the faster the water cut rose after water breakthrough, and the lower the recovery degree corresponding to the same water cut became.

The model with $\theta = 0°$ was selected to study the effect of the fracture length on the water saturation because the impact of large-scale fractures on the water saturation was the most significant at this angle. With L = 30 m, the influence of different large-scale fracture lengths on the distribution of the water saturation was examined. Fig. 20 shows the saturation distributions corresponding to different fracture length models during production.

The analysis and calculation in Fig. 21 showed that as the length of the large-scale fracture increased, the water intrusion time of the production well increased. After the water cut occurred, the water content increased faster, but the increase rate slowed later. Furthermore, the longer the large-scale fracture length was, the lower the degree of recovery become.

As shown in Fig. 22, in the large-scale complex fracture model, due to the high conductivity of large-scale fractures and the higher fluidity of the water phase, when the frontal edge of the two-phase zone reached the large-scale fracture, the water phase rapidly advanced along the large-scale fracture, causing the water cut of the production well to increase quickly, and forming an oil-rich zone at the edge of the large-scale fracture. With the extension of the water injection time, the frontal edge shape of the two-phase area was divided by the large-scale fracture, resulting in non-uniform displacement. This is the reason that, compared with homogeneous reservoirs under the same geological environment and production conditions, fractured reservoirs undergo early water seepage and low recovery.
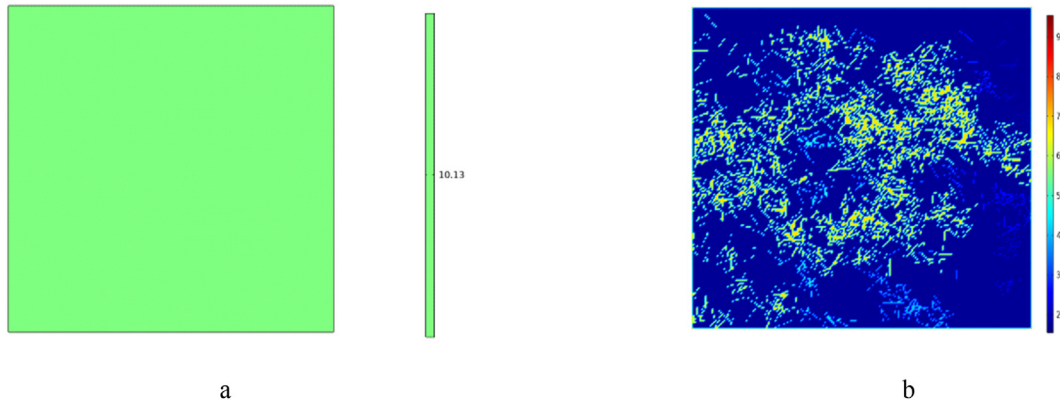
**Fig. 13.** Permeability field distribution in the matrix−microfracture system: a. matrix permeability (mD) and b. microfracture permeability (mD).



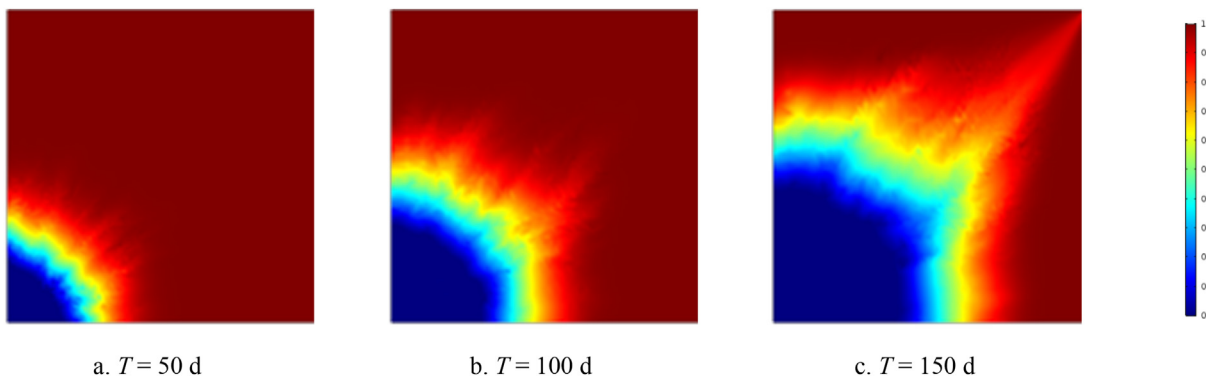a. $T = 50$ d    b. $T = 100$ d    c. $T = 150$ d

**Fig. 14.** Water saturation distribution diagrams in the matrix−microfracture system at different times when the $D_C$ value of the microfractures was 1.75.
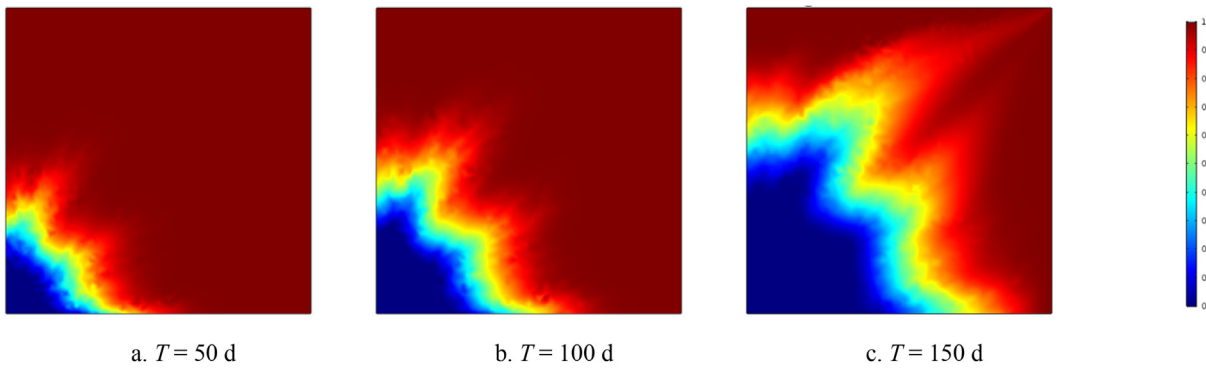


a. $T = 50$ d    b. $T = 100$ d    c. $T = 150$ d

**Fig. 15.** Water saturation distribution diagrams in the matrix−microfracture system at different times when the $D_C$ value of the microfractures was 1.45.

The analysis discussed above established that the large-scale fractures had a greater effect on the water saturation than the microfractures. Modeling large-scale fractures and microfractures at the same time would greatly increase the modeling difficulty and calculation cost. For the area studied in this work, when the fracture correlation dimension was greater than 1.8, due to the dominant effect of the large-scale fractures, microfractures could be reasonably ignored. The resulting water breakthrough time error was 5%−13%, depending on the shape and location of the microfracture cluster area. However, determining whether this guideline is universal still needs to be verified in combination with the distribution of fractures in different areas.

## 6. Conclusions

Multiple techniques, including the finite volume method, fractal theory, ant tracking, and image analysis, were employed to build a multiphase flow model in a multi-scale fractured reservoir. Its numerical solution was obtained, and the influences of microfractures and large-scale fractures on the water saturation distribution were analyzed. The main conclusions of this work can be summarized as follows:

(1) The dimensionality reduction method is a potential fracture treatment method because it can effectively avoid the generation of a minimized grid, but the flow discontinuity
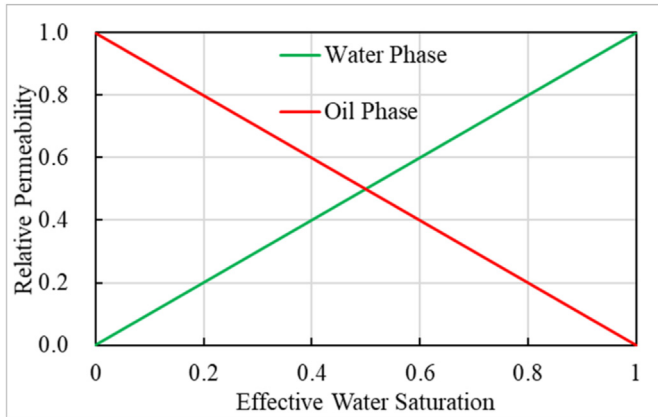
**Fig. 16.** Relative permeability curves of large-scale fracture system.

problem restricts the application of this method. By introducing a dimensionless aperture operator, the problem of large-scale fracture flow discontinuity caused by the dimensionality reduction method was effectively solved.

(2) Due to the saturation step phenomenon at a fracture interface at a leading edge of the water flooding, a higher-order upwind scheme should be used to differentiate saturation and fluidity. The modified higher-order upwind scheme proposed in this paper can effectively suppress the non-physical oscillations of the saturation at a large-scale fracture interface and improve the accuracy of its solution.

(3) The case study results showed that fracture systems of different scales had an impact on a distribution of the water saturation. The microfracture system increased the tortuosity of an oil−water front. According to the analysis results for microfractures with different correlation dimensions, the
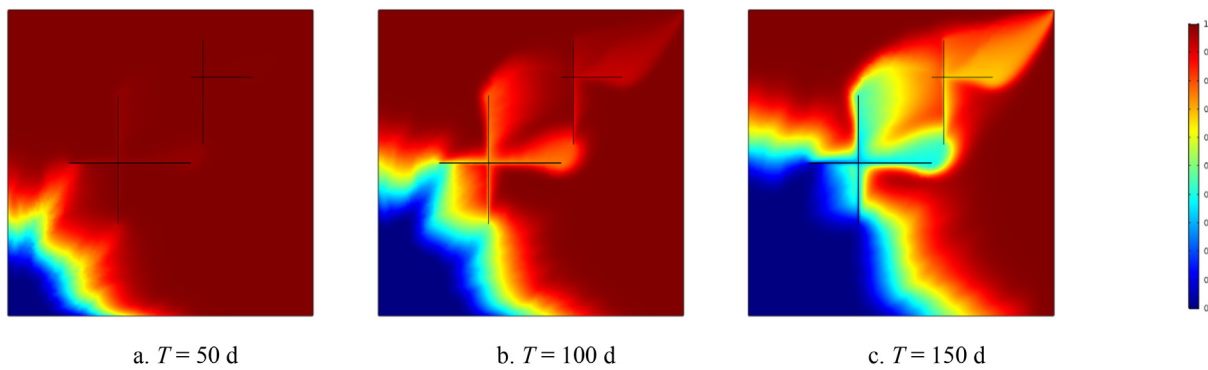


a. $T = 50$ d  　　　　 b. $T = 100$ d  　　　　 c. $T = 150$ d

**Fig. 17.** Water saturation distribution diagrams of the multiscale fracture system at different times.



a. $\theta = 0°$  　　　　 b. $\theta = 45°$  　　　　 c. $\theta = 90°$

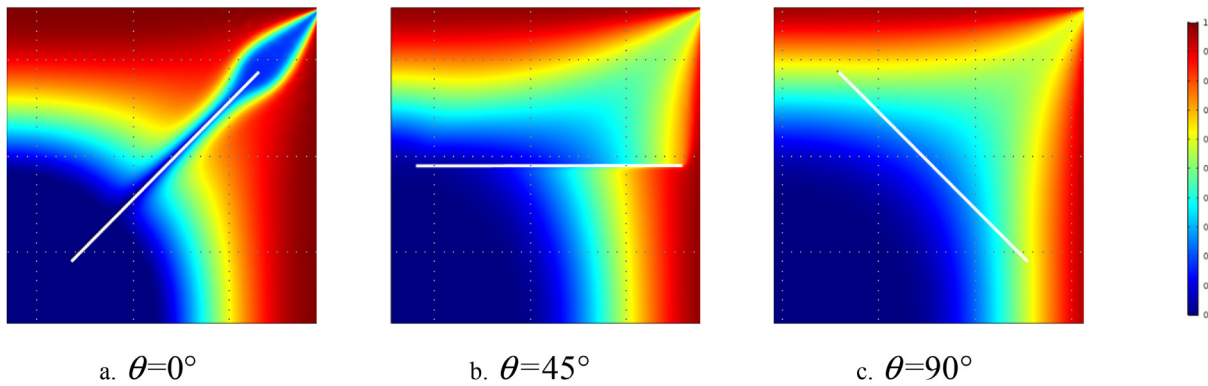**Fig. 18.** Control effect of the direction of large-scale fractures on the distribution of water saturation.
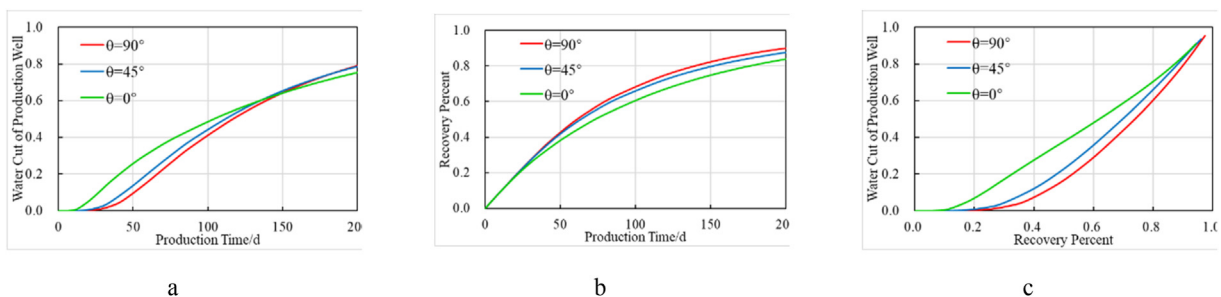


a  　　　　　　　　　b  　　　　　　　　　c

**Fig. 19.** Influence of the direction of large-scale fractures on the water cut and recovery of production wells: a. influence of fracture direction on water appearance time, b. influence of fracture direction on the recovery percent, and c. water content corresponding to different recovery percentages.
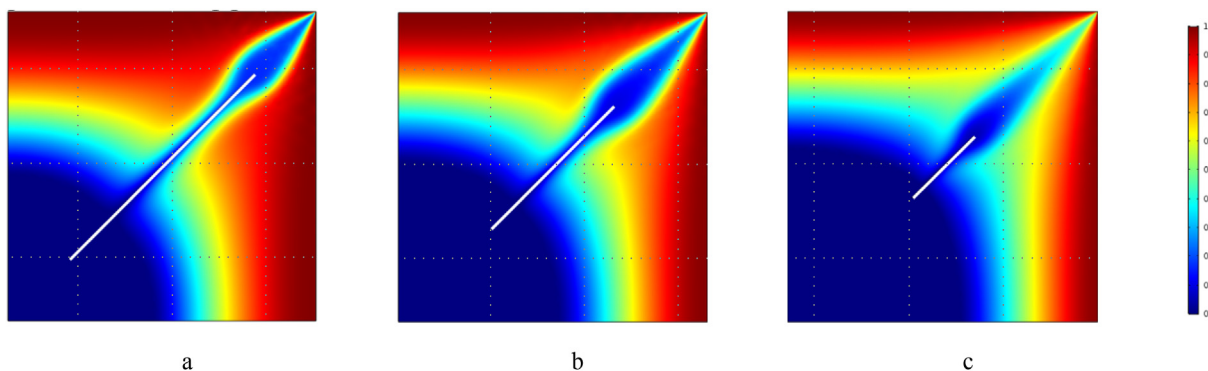
a  b  c

**Fig. 20.** Control effect of the lengths of large-scale fractures on the distribution of water saturation with large-scale fracture lengths of a. 3*L*, b. 2*L*, and c. *L*.
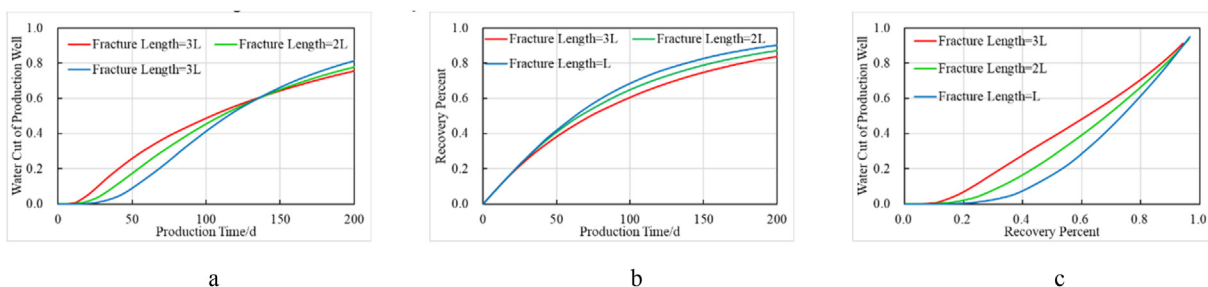


a  b  c

**Fig. 21.** Influence of the lengths of the large-scale fractures on the water cut and recovery of production wells: a. influence of fracture length on water cut, b. influence of fracture length on the recovery percent, and c. water content corresponding to different recovery percentages.
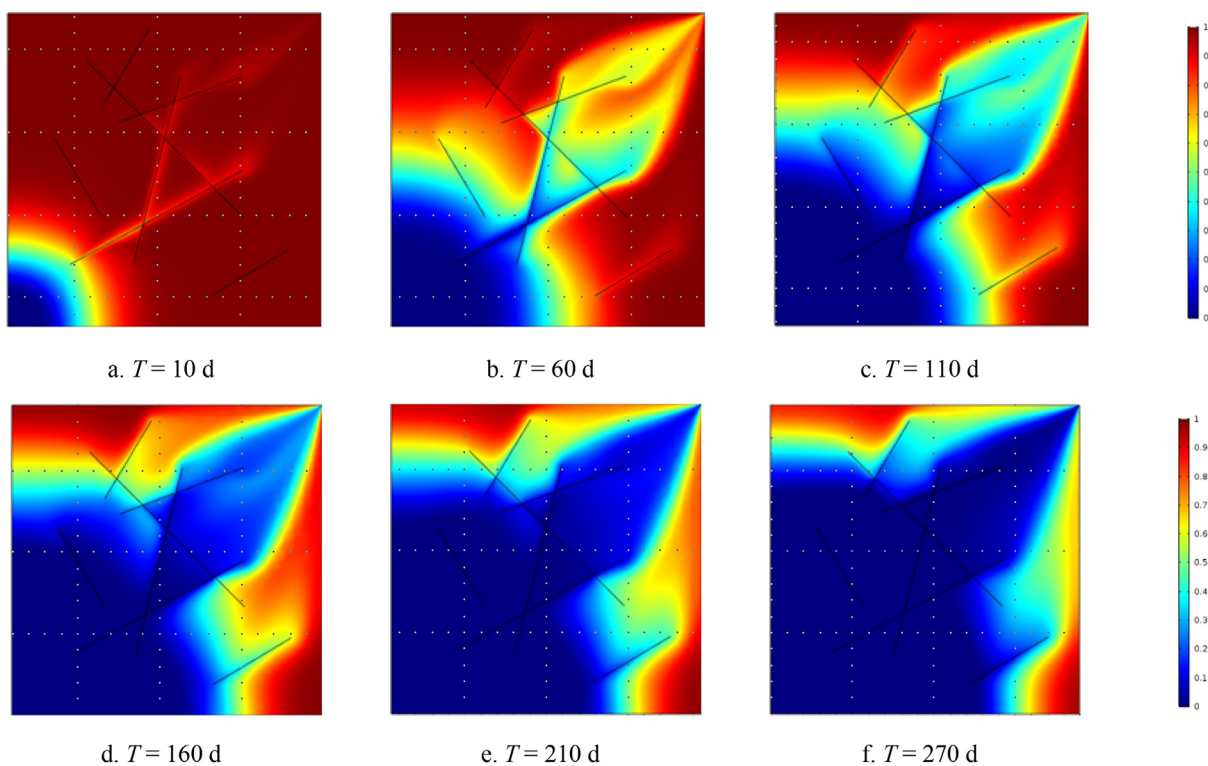


a. *T* = 10 d  b. *T* = 60 d  c. *T* = 110 d

d. *T* = 160 d  e. *T* = 210 d  f. *T* = 270 d

**Fig. 22.** Effect of the multi-scale fracture system on the water saturation at different times.

smaller the correlation dimension of a microfracture network, the greater the tortuosity of the oil−water front. Targeted well pattern adjustments should be made for areas of microfracture development during reservoir development.

(4) Compared to microfractures, the effect of large-scale fractures on the water saturation is more significant. When an oil−water front reaches large-scale fractures, the large-scale fractures will cut the oil−water front, which will significantly increase the heterogeneity of a displacement process. In the development process, the large-scale fracture orientation and length should be identified as early as possible, and production wells should be arranged in a direction perpendicular to the fractures, thereby extending the water-free oil production period.

## Declaration of competing interest

The authors declare that they have no conflicts of interest.

## Acknowledgments

## Nomenclature

*English alphabet*

| | |
|---|---|
| $B$ | volume factor |
| $d$ | dimensionless fracture aperture |
| $\mathbf{e}$ | unit vector |
| $h$ | perforation length |
| $K$ | permeability |
| $l$ | length |
| $\mathbf{n}$ | unit normal vector |
| $\mathbf{v}$ | velocity vector |
| $\mathbf{S}$ | surface vector |
| $s$ | saturation |
| $p$ | pressure |

*Greek alphabet*

| | |
|---|---|
| $\alpha$ | shape factor |
| $\beta$ | characteristic coefficient of the medium |
| $\varphi$ | porosity |
| $\lambda$ | fluidity |
| $\mu$ | viscosity |
| $\rho$ | density |
| $\Phi$ | variable value |

*Subscript*

| | |
|---|---|
| c | capillary |
| C | control element |
| e | effective |
| f | microfracture |
| F | large-scale fracture |
| m | matrix |
| o | oil |
| r | relative permeability |
| w | water |

## Credit author statement

**Chao Tang:** Software, Writing − original draft preparation, Validation. Wen Zhou: Supervision. **Zhimin Du:** Conceptualization, Methodology. **Zhangxing Chen:** Writing-Reviewing and Editing. **Jiabao Wei:** Data curation, Visualization, Investigation.

## References

[1] Aljuboori FA, Lee JH, Elraies KA, Stephen KD. The effectiveness of low salinity waterflooding in naturally fractured reservoirs. J Petrol Sci Eng 2020;191: 107167.

[2] Li J, Chen Z. On the semi-discrete stabilized finite volume method for the transient Navier−Stokes equations. Adv Comput Math 2013;38:281−320.

[3] Adler PM, Thovert JF, Mourzenko VV. Fractured porous media, vol. 38. Oxford: Oxford University Press; 2012.

[4] Bear J, Tsang CF, De Marsily G. Flow and contaminant transport in fractured rock. Cambridge: Academic Press; 2012.

[5] Faybishenko B, Benson S, Gale JJE. Dynamics of fluids and transport in complex fractured-porous systems. Hoboken: Wiley; 2015.

[6] Illman WA. Hydraulic tomography offers improved imaging of heterogeneity in fractured rocks. Groundwater 2014;52(5):659−84.

[7] Neuman SP. Trends, prospects and challenges in quantifying flow and transport through fractured rocks. Hydrogeol J 2005;13:124−47.

[8] Berre I, Doster F, Keilegavlen E. Flow in fractured porous media: a review of conceptual models and discretization approaches. Transport Porous Media 2019;130(1):215−36.

[9] Mozolevski I, Schuh LA. Numerical simulation of two-phase immiscible incompressible flows in heterogeneous porous media with capillary barriers. J Comput Appl Math 2013;242:12−27.

[10] Rong G, Peng J, Wang X, Liu G, Hou D. Permeability tensor and representative elementary volume of fractured rock masses. Hydrogeol J 2013;21:1655−71.

[11] Hunt AG, Sahimi M. Flow, transport, and reaction in porous media: percolation scaling, critical-path analysis, and effective medium approximation. Rev Geophys 2017;55:993−1078.

[12] Ranjbar E, Hassanzadeh H, Chen Z. Effect of fracture pressure depletion regimes on the dual-porosity shape factor for flow of compressible fluids in fractured porous media. Adv Water Resour 2011;34:1681−93.

[13] Ruiz G, Ortiz M, Pandolfi A. Three-dimensional finite-element simulation of the dynamic Brazilian tests on concrete cylinders. Int J Numer Methods Eng 2000;48:963−94.

[14] Rostami P, Sharifi M, Dejam M. Shape factor for regular and irregular matrix blocks in fractured porous media. Petrol Sci 2019;17:136−52.

[15] Watanabe N, Sakurai K, Ishibashi T, Ohsaki Y, Tamagawa T, Yagi M, Tsuchiya N. New ν-type relative permeability curves for two-phase flows through subsurface fractures. Water Resour Res 2015;51:2807−24.

[16] Su SH, Gosselin OR, Parvizi H, Giddins MA. Dynamic matrix-fracture transfer behavior in dual-porosity models. 2013 [Eurosurveillance].

[17] Wang K, Liu H, Luo J, Wu K, Chen Z. A comprehensive model coupling embedded discrete fractures, multiple interacting continua and geomechanics in shale gas reservoirs with multi-scale fractures. Energy Fuel 2017;31: 7758−76.

[18] Zheng H, Shi A, Liu Z, Wang X. A dual-porosity model considering the displacement effect for incompressible two-phase flow. Int J Numer Anal Methods GeoMech 2020;44:691−704.

[19] Tecklenburg J, Neuweiler I, Dentz M, Carrera J, Geiger S, Abramowski C, Silva O. A non-local two-phase flow model for immiscible displacement in highly heterogeneous porous media and its parametrization. Adv Water Resour 2013;62:475−87.

[20] March R, Doster F, Geiger S. Assessment of $CO_2$ storage potential in naturally fractured reservoirs with dual-porosity models. Water Resour Res 2018;54(3): 1650−68.

[21] Sandve TH, Berre I, Nordbotten JM. An efficient multi-point flux approximation method for discrete fracture-matrix simulations. J Comput Phys 2012;231:3784−800.

[22] Yongming H, Chen X, Zhang Y, Yu W. Modeling interporosity flow functions and shape factors in low-permeability naturally fractured reservoir. J Petrol Sci Eng 2017;156:110−7.

[23] Zheng H, Wang M, Wang X. Exchange flow numerical method of dual-porosity model for different matrix size in 2D oil-water imbibition. J Phys Conf 2020;1549(3):032026.

[24] Sahimi M. Characterization of fractures and fracture network of porous media.

Handbook of porous media. CRC Press; 2015. 2015.

[25] Liu R, Li B, Jiang Y, Huang N. Mathematical expressions for estimating equivalent permeability of rock fracture networks. Hydrogeol J 2016;24(7): 1623−49.

[26] Liu YW, Gao DP, Li Q, et al. Mechanical frontiers in shale-gas development. Adv Mech 2019;49:201901. 2019.

[27] Moinfar AA, Varavei A, Sepehrnoori K, Johns RT. Development of an efficient embedded discrete fracture model for 3D compositional reservoir simulation in fractured reservoirs. SPE J 2014;19:289−303.

[28] Moinfar AA, Varavei A, Sepehrnoori K, Johns RT. Development of a coupled dual continuum and discrete fracture model for the simulation of uncon- ventional reservoirs. ANSS 2013. 2013.

[29] Møyner O. Next generation multiscale methods for reservoir simulation. 2016.

[30] Blunt MJ, Bijeljic B, Dong H, Gharbi O, Iglauer S, Mostaghimi P, Paluszny A, Pentland CH. Pore-scale imaging and modelling. Adv Water Resour 2013;51: 197−216.

[31] Bonneau F, Caumon G, Renard P. Impact of a stochastic sequential initiation of fractures on the spatial correlations and connectivity of discrete fracture networks. J Geophys Res 2016;121:5641−58.

[32] Rajeh T, Ababou R, Marcoux M, Cañamón I. Fast upscaling of the hydraulic conductivity of three-dimensional fractured porous rock for reservoir modeling. Math Geosci 2019;1−38.

[33] Xu Peng, Li Cuihong, Qiu Shuxia. A fractal network model for fractured porous media. Fractals 2016;24(2):1650018.

[34] Merland R, Caumon G, Lévy B, Collon-Drouaillet P. Voronoi grids conforming to 3D structural features. Comput Geosci 2014;18(3−4):373−83.

[35] Tene M, Bosma S, Kobaisi MS, Hajibeygi H. Projection-based embedded discrete fracture model (pEDFM). Adv Water Resour 2017;105:205−16.

[36] Moukalled F, Mangani L, Darwish M. High resolution schemes. 2016.

[37] Xu P, Qiu S, Yu B, Jiang Z. Prediction of relative permeability in unsaturated porous media with a fractal approach. Int J Heat Mass Tran 2013;64:829−37.

[38] K. Fluid flow in fractured rock: theory and application. 2012.

[39] Zadhesh J, Jalali SME, Ramezanzadeh A. Estimation of joint trace length probability distribution function in igneous, sedimentary, and metamorphic rocks. Arab J Geosci 2014;7(6):2353−61.

[40] Riquelme AJ, Abellán A, Tomás R, Jaboyedoff M. A new approach for semi- automatic rock mass joints recognition from 3D point clouds. Comput Geo- sci 2014;68:38−52.

[41] Sandve TH, Berre I, Nordbotten JM. An efficient multi-point flux approxima- tion method for discrete fracture-matrix simulations. J Comput Phys 2012;231:3784−800.

[42] Brenner K, Hennicker J, Masson R, Samier P. Hybrid-dimensional modelling of two-phase flow through fractured porous media with enhanced matrix fracture transmission conditions. J Comput Phys 2018;357:100−24.

[43] Chen Z, Zhang Y. Well flow models for various numerical methods. Int J Numer Anal Model 2009;6(3).

[44] Chung ET, Efendiev YR, Leung T, Vasilyeva MV. Coupling of multiscale and multi-continuum approaches. GEM Int J Geomath 2017;8:9−41.

[45] Patankar S. Numerical heat transfer and fluid flow. Taylor & Francis; 2018.

[46] Dumbser M, Käser M. Arbitrary high order non-oscillatory finite volume schemes on unstructured meshes for linear hyperbolic systems. J Comput Phys 2007;221:693−723.

[47] Chen H, Kou J, Sun S, Zhang T. Fully mass-conservative IMPES schemes for incompressible two-phase flow in porous media. Comput Methods Appl Mech Eng 2019;350:641−63.